

The Dependence of Tropical Modes of Variability on Zonal Asymmetry

Xiaoning Wu¹, Kevin A. Reed¹, Christopher L. P. Wolfe¹, Gustavo M. Marques², Scott D. Bachman², Frank O. Bryan²

¹School of Marine and Atmospheric Sciences, Stony Brook University, Stony Brook, NY

²Climate and Global Dynamics Laboratory, National Center for Atmospheric Research, Boulder, CO

Key Points:

- Two idealized coupled models, with and without a meridional ocean boundary, show MJO- and ENSO-relevant modes of tropical variability
- Without zonal asymmetry, the MJO-like intraseasonal mode becomes less distinct from equatorial Kelvin waves
- Without the ocean's meridional boundary, the ENSO-like interannual mode still persists around the equator but with different dynamics

Corresponding author: Xiaoning Wu, xiaoning.wu.1@stonybrook.edu

Abstract

Tropical modes of variability, including the Madden-Julian Oscillation (MJO) and the El Niño-Southern Oscillation (ENSO), are challenging to represent in climate models. Previous studies suggest their fundamental dependence on zonal asymmetry, but such dependence is rarely addressed with fully coupled ocean dynamics. This study fills the gap by using fully coupled, idealized Community Earth System Model (CESM) and comparing two nominally ocean-covered configurations with and without a meridional boundary. For the MJO-like intraseasonal mode, its separation from equatorial Kelvin waves and the eastward propagation of its convective and dynamic signals depend on the zonal gradient of the mean state. For the ENSO-like interannual mode, in the absence of the ocean’s meridional boundary, a circum-equatorial dominant mode emerges with distinct ocean dynamics. The interpretation of the dependence of these modes on zonal asymmetry is relevant to their representation in realistic climate models.

Plain Language Summary

In Earth’s tropical regions, recurring patterns — such as El Niño and atmospheric waves that come with storm clusters — have a large influence on the global weather and climate. These patterns are also challenging to represent in modern climate models. Previous studies suggest that the behavior of these patterns depends on the east-west contrast in the Pacific ocean, but these studies typically focus on the atmosphere while ignoring relevant actions in the ocean, or vice versa. In this study, we address the question by using a state-of-the-art climate model with a full-blown atmosphere and ocean. We compare two designs with simplified continental shapes, one with east-west contrast and the other without. The behavior of atmospheric waves is more realistic with an east-west contrast. On the other hand, in a global ocean with no land blocking the east-west direction and therefore no east-west contrast, phenomena similar to El Niño can still occur around the equator, but with different ocean processes. Understanding the essential conditions for these patterns will contribute to better climate models for prediction, helping with the preparation for and mitigation of extreme weather and climate events.

1 Introduction

Tropical modes of variability in Earth’s climate system, such as the Madden-Julian Oscillation (MJO) and the El Niño-Southern Oscillation (ENSO), have global relevance for climate prediction and projection over various timescales. Yet they remain challenging to represent in state-of-the-art climate models (e.g., Hung et al., 2013; Chen et al., 2017). Over time, model development has generally led to encouraging improvements in their representation (G. Wang et al., 2015; Ahn et al., 2020). However, the complexity of contemporary, full-fledged Earth system models often obscures the sources of improvement (or lack thereof) regarding various aspects or processes (see, e.g., discussion in Bayr et al., 2019; Klingaman & Demott, 2020; Planton et al., 2021). Studying these modes of variability in an idealized framework can facilitate the understanding of their behavior in more complex models. For example, idealized models have been used to study the role of the Pacific mean state — including the zonal gradients in the atmosphere and the ocean — in setting the dynamics of both MJO (e.g., Maloney & Wolding, 2015; Leroux et al., 2016; Das et al., 2019) and ENSO (e.g., Clement et al., 2011; Battisti et al., 2019).

For MJO, a review of its current understanding and modeling challenges is provided by Jiang, Adames, et al. (2020). The role of zonally asymmetric heating by the western Pacific warm pool has been addressed by idealized studies emphasizing the atmospheric component. Through the comparison of atmosphere-only aquaplanet experiments with and without an imposed western warm pool, it is suggested that the zonal asymmetries in both moisture and background mean flow are crucial for realistic features of MJO (Landu

& Maloney, 2011; Maloney & Wolding, 2015), although such effects may be model-dependent (Leroux et al., 2016). Das et al. (2019) suggests that the zonal asymmetry in sea surface temperature (SST) is likely more important than the sole presence of continents. Meanwhile, studies using zonally symmetric prescribed SST have explored aspects of sensitivity, including the influences of moisture asymmetry (Hsu et al., 2014), interactive surface evaporation (Shi et al., 2018), and the large-scale background state (Jiang, Maloney, & Su, 2020). On a specific note, although the role of an active ocean component has been suggested for MJO dynamics (e.g., DeMott et al., 2015, and references therein), idealized modeling studies are relatively scarce (e.g., Grabowski, 2006; Maloney & Sobel, 2007, with slab ocean models), and hardly any involves full ocean dynamics.

For ENSO, a brief history of its quintessential dynamic models and outlooks for comprehensive modeling are reviewed in Section 4 of Battisti et al. (2019). With regard to idealization, the first models of ENSO theory and prediction are typically “box-shaped” representations of the Pacific (e.g., Zebiak & Cane, 1987; Battisti, 1988; Schopf & Suarez, 1988). In these classic models with simplified dynamics and minimal physics, the meridional boundary is indispensable for the dynamical adjustment of the equatorial ocean that maintains the interannual oscillation: a sensitivity experiment in Battisti (1988) suggests that the removal of the meridional boundary may result in unconstrained growth of warming, due to the lack of a phase-switching mechanism that counteracts the positive Bjerknes feedback. In contemporary climate models, these ocean dynamics are generally considered necessary for modeling realistic ENSO records (Chen et al., 2017; Planton et al., 2021). On the other hand, reduced-complexity modeling studies have revealed unexpected and intriguing aspects of ENSO-relevant model behaviors affecting interannual timescales, independent of explicit ocean dynamics that require a meridional boundary or zonal asymmetry. For example, studies using slab-ocean models (e.g., Clement et al., 2011; Dommenges et al., 2014) suggest that in the absence of ocean dynamics, feedbacks associated with wind-driven evaporation and cloud radiative effects can lead to realistic ENSO-like behavior in the atmospheric component. Additionally, using a global radiative-convective equilibrium model coupled to a slab ocean — which explicitly excludes zonal asymmetry — Coppin and Bony (2017) suggest that internal variability due to feedbacks between SST and convective aggregation can arise on interannual timescales when the ocean is sufficiently deep. More generally, this behavior is associated with the ocean’s role in transferring — or “reddening” — stochastic atmospheric variability on synoptic timescales into climate variability on interannual or longer timescales (e.g., Hasselmann, 1976). Although their existence does not explicitly depend on zonal asymmetry, this type of mechanisms is suggested to affect ENSO (e.g., Perez et al., 2005, using a “box-shaped” simplified Pacific model).

In short, although the fundamental dependence of intraseasonal and interannual modes of tropical variability on zonal asymmetry has been partially addressed by previous works, fully coupled ocean dynamics have generally not been considered. In this study, we explore this question in a fully coupled context. This is done by taking advantage of the newly available idealized and fully coupled configurations of the Community Earth System Model (CESM; Hurrell et al., 2013; Danabasoglu et al., 2020). The design of two idealized configurations and their mean states are documented in detail in Wu et al. (2021, hereafter W21). In the mean state, the zonally asymmetric Ridge configuration — with a single grid-cell-wide meridional boundary for the ocean — is a box-shaped approximation of the Pacific, with the zonal gradient between the western warm pool and eastern cold tongue, and the associated Walker-like circulation. In contrast, the zonally symmetric Aqua configuration — nominally ocean-covered like conventional atmospheric aquaplanets, but coupled to a dynamical ocean — develops a global cold belt of wind-driven equatorial upwelling. For both the intraseasonal and interannual modes, the role of zonal asymmetry is examined in perhaps the most straightforward manner possible by comparing the emergent dynamics when the meridional boundary is present (Ridge) or not (Aqua). Through the exploration, we aim to highlight the aspects through

which zonal asymmetry in the mean state affects the MJO- and ENSO-like modes of variability. With an idealized approach, improved understanding of these aspects will have broader relevance for the interpretation and improvement of the representation of these modes of variability in comprehensive, fully coupled models.

2 Model and Data

The two idealized models are configured using CESM (Hurrell et al., 2013; Danabasoglu et al., 2020), with fully coupled atmosphere, ocean, sea ice, and land components. The Ridge configuration (similar to Smith et al., 2006; Enderton & Marshall, 2009) is zonally bounded by a single strip of pole-to-pole continent. The Aqua configuration, without the meridional boundary, is nominally ocean-covered and zonally symmetric.

The model design is described in detail in W21. By Year 400, both models reach quasi-equilibrium climate states (see W21 for details). Due to computational and storage constraints for archiving model outputs at high temporal resolution, the results in Section 3.1 are based on 6-hourly output of the atmosphere over the 20-year record of Year 401–420. The results in Section 3.2 use monthly averaged output of the atmosphere and annually averaged output of the ocean over the 100-year record of Year 401–500.

3 Results

3.1 Convectively Coupled Equatorial Waves and Intraseasonal Variability

The Ridge configuration captures a range of features of convectively coupled equatorial waves (CCEWs) and MJO qualitatively consistent with Earth observations. Fig. 1 shows the vertical profiles of climatological zonal wind averaged between 15°N–15°S, and Wheeler-Kiladis diagrams (Wheeler & Kiladis, 1999) based on 6-hourly precipitation. Throughout most vertical levels, Ridge’s background zonal flow is relatively weak at $\sim -5 \text{ m s}^{-1}$ or lower (Fig. 1a). Therefore, the zero-mean-flow approximation typical for the dispersal relations of CCEWs in the Wheeler-Kiladis diagrams is reasonably adequate (solid black curves in Fig. 1b and d). In the symmetric component (Fig. 1b), spectral signals corresponding to equatorial Rossby and Kelvin waves are present. An MJO-like mode with periodicity beyond 20 days is separated from the equatorial Kelvin waves, reaching zonal wave numbers 3–4 (dark blue box in Fig. 1b). In the antisymmetric component (Fig. 1d), signals corresponding to mixed Rossby-gravity and inertia-gravity waves are also present.

Focusing on the MJO-like mode, Fig. 2 shows its propagation embedded in the mean state. The climatological precipitation of the Ridge configuration (Fig. 2a) is shaped by the climatological SST (Fig. 2f in W21). Two ITCZs converge towards the western warm pool, and the relatively dry region over the eastern cold tongue reflects the descending branch of the Walker-like circulation (Fig. 2b in W21). Following Waliser et al. (2009), the MJO-like mode is extracted by band pass filtering the precipitation and low-level zonal wind at 850 hPa to retain only motions with periods between 20 and 100 days. The propagation of this mode is then examined using lagged correlation across both the zonal (Fig. 2c) and meridional (Fig. 2e) directions. The reference region of the lagged correlation, marked by the orange box in Fig. 2a, is chosen on the western side of the climatological warm pool, loosely analogous to the Indian Ocean for observed MJO (Waliser et al., 2009; Ahn et al., 2017). In the zonal direction (Fig. 2c), the intraseasonal precipitation anomaly shows coherent eastward propagation over local centers of maximum climatological precipitation near 90°E around the climatological warm pool before decaying. The dynamic anomaly, as represented by intraseasonal low-level zonal wind, lags behind the precipitation anomaly by ~ 5 days west of $\sim 90^\circ\text{E}$. As the precipitation anomaly decays east of $\sim 90^\circ\text{E}$, the zonal wind anomaly shows increased phase speed over the drier region. In

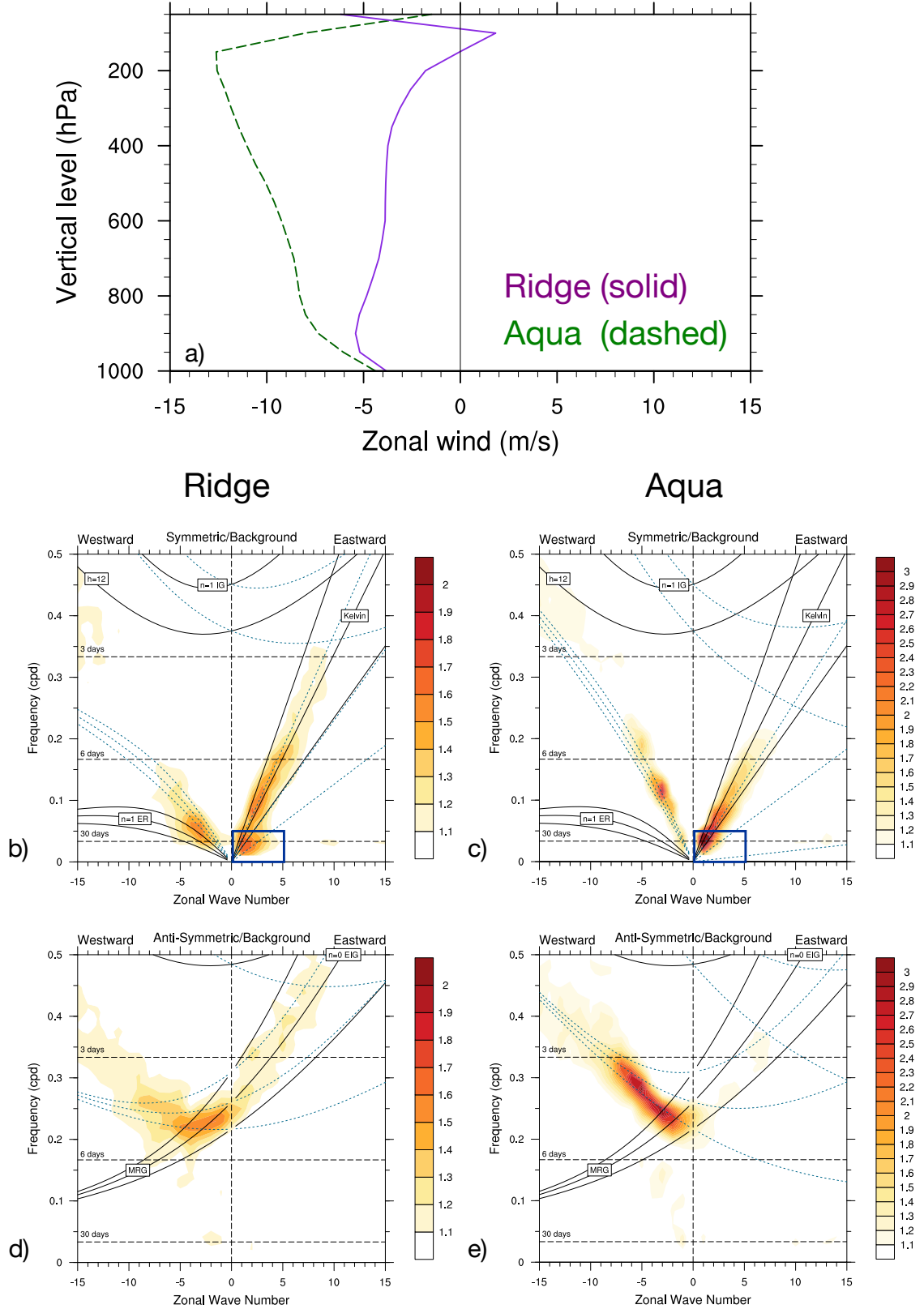


Figure 1. The interaction between zonal mean flow and convectively coupled equatorial waves, using data from Yr 401–420. (a) Vertical profiles of the zonal mean zonal wind, averaged between 15°N–15°S; (b–e) Wheeler-Kiladis diagrams of 6-hourly precipitation, averaged between 15°N–15°S. The solid black curves represent the theoretical dispersal relations assuming zero zonal flow, whereas the dashed blue curves represent the dispersal relations Doppler-shifted by the background zonal flow of -5 m s^{-1} for Ridge (b and d), and -10 m s^{-1} for Aqua (c and e).

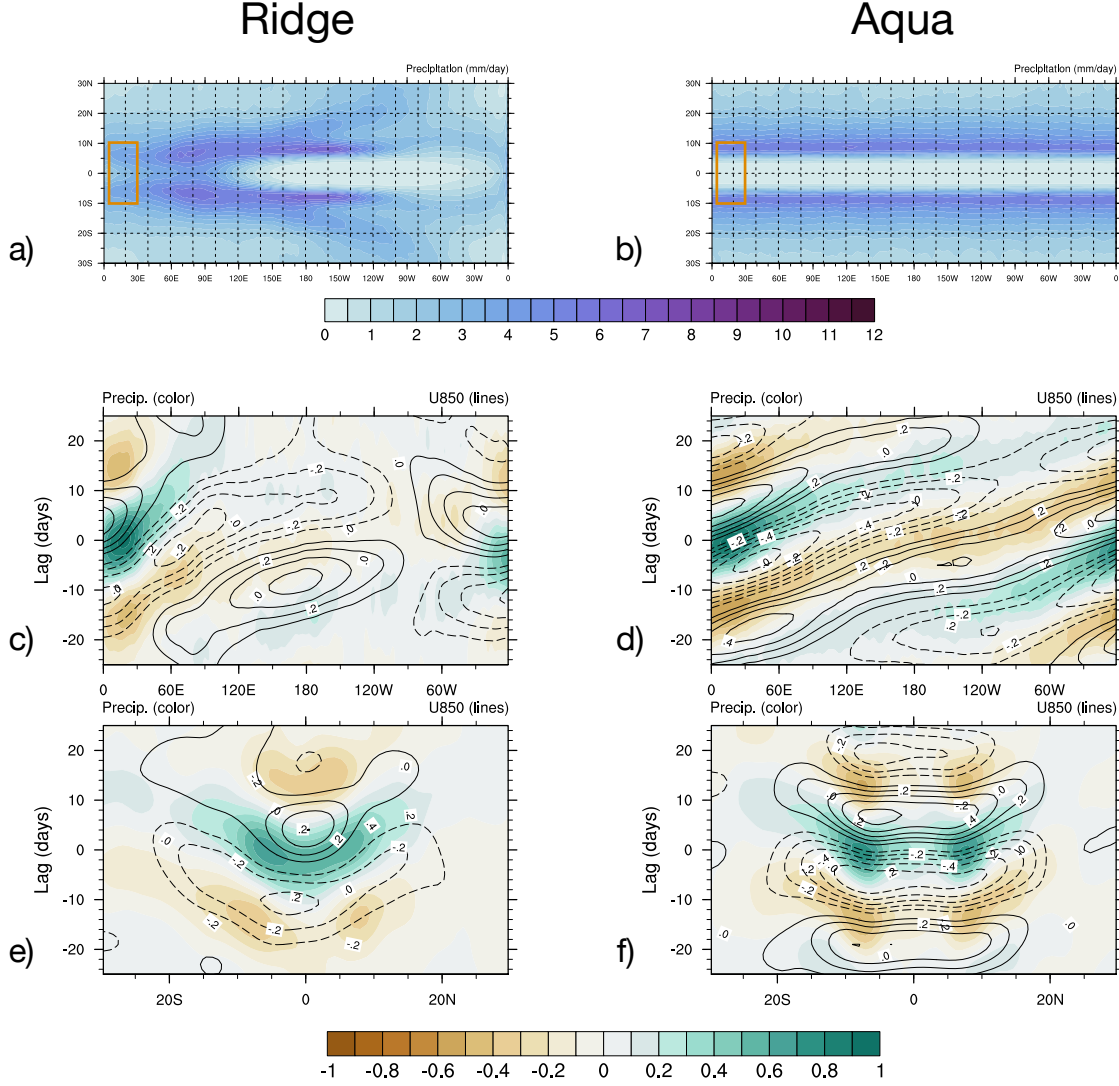


Figure 2. The propagation of the MJO-like mode, using data from Yr 401–420. (a–b) The climatology of annual average precipitation (m day^{-1}); (c–f) Lagged correlation of the filtered signal with 20–100 day period in precipitation (colored shading) and low-level zonal wind at 850 hPa (contour), across the zonal direction (c–d) and meridional direction (e–f). The orange box of 10°N – 10°S , 5° – 30°E in (a–b) marks the reference location of the lagged correlation in (c–f).

the meridional direction (Fig. 2e), both the precipitation anomaly and the zonal wind anomaly show poleward propagation; the equatorward contraction of the centers of maximum lagged correlation in precipitation reflects the zonal structure of the underlying climatology. These characteristics are qualitatively consistent with the propagation of observed MJO over the Pacific (cf. Fig. 5 and 6 in Waliser et al., 2009). It is also worth mentioning that the qualitative features of the lagged correlation discussed above are not sensitive to the exact longitude of the reference region in Fig. 2a, as long as its general position relative to the climatological warm pool is maintained.

In the Aqua configuration where zonal asymmetry is removed, an intraseasonal mode still exists, although the characteristics of this mode as well as the CCEWS are notably affected. Aqua’s background easterly flow is substantially stronger than Ridge through-

out almost all the vertical levels, reaching beyond $\sim -10 \text{ m s}^{-1}$ in the upper levels (Fig. 1a). As a result, in the Wheeler-Kiladis diagrams (Fig. 1c and e), the westward signals are not well approximated by the theoretical dispersal relations of equatorial Rossby or mixed Rossby-gravity waves assuming zero background velocity. This is largely due to Doppler-shifting by the background zonal flow (e.g., regional observation discussed by Dias & Kiladis, 2014), i.e., the frequency $\hat{\omega}$ of motions observed in an Eulerian frame is different from the true frequency, ω , in the presence of a nonzero background velocity, \mathbf{U} (see e.g., Ch. 11 in Gill, 1982):

$$\hat{\omega} = \omega - \mathbf{U} \cdot \mathbf{k}. \quad (1)$$

Accounting for the background flow by incorporating a zonal velocity of -10 m s^{-1} , dispersion relations are generated that align with the empirical signals (dashed blue curves in Fig. 1c and e). In comparison to Aqua (Fig. 1c and e), a background mean flow of -5 m s^{-1} is incorporated for Ridge (dashed blue curves in Fig. 1b and d) to demonstrate the smaller effects arising from the mean easterly flow. Note that for either configuration, the magnitude of the background zonal velocity is a qualitative indication rather than a precise estimate (see e.g., discussion in Dias & Kiladis, 2014, on the considerations for such estimates). For Aqua’s intraseasonal mode with periodicity beyond 20 days (dark blue box in Fig. 1c), its separation from the equatorial Kelvin waves becomes less distinct than in the Ridge configuration, with reduced zonal wave numbers.

For consistency, Aqua’s intraseasonal mode is diagnosed in the same manner as the Ridge configuration in Fig. 2. As discussed in W21, the climatological precipitation of the Aqua configuration (Fig. 2b) shows two ITCZs around 10°N/S that correspond to the locations of SST maxima, and a cold and dry equatorial belt where precipitation is suppressed by the descending branch of the “reverse Hadley” circulation (see Fig. 4b and 8a in W21). Given the zonal uniformity of the Aqua configuration, the longitude of the reference region for the lagged correlation is entirely arbitrary, and coordinates identical to that of the Ridge configuration are used (the orange box in Fig. 2b). In the zonal direction (Fig. 2d), the propagation of the precipitation anomaly likewise leads the zonal wind anomaly by ~ 5 days. The contrast with Ridge is in line with what the mean state might imply: without the zonal gradient in moisture, the phase speed of the zonal wind anomaly becomes nearly zonally uniform, and the propagation of precipitation anomaly becomes more persistent. In the meridional direction (Fig. 2f), both of the anomalies likewise propagate poleward, and without Ridge’s zonal structure, the centers of maximum lagged correlation in precipitation remain around the latitude of the climatological double ITCZs.

The comparison above suggests dynamic and thermodynamic aspects through which zonal asymmetry affects CCEWs and the MJO-like intraseasonal mode. For CCEWs, Aqua’s zonal symmetry produces stronger background mean easterlies in the tropics, leading to more pronounced Doppler-shifting in the dispersal relations. For the MJO-like intraseasonal mode, Ridge’s zonal structure of the thermodynamic environment in the mean state is essential for the dynamic and convective structure of this mode. These factors likely affect the separation of this mode from equatorial Kelvin waves: in the Ridge configuration its spatial scale is constrained by the climatological warm pool, whereas in Aqua’s zonally uniform double ITCZs, this spatial constraint is removed, resulting in reduced zonal wave numbers.

3.2 Equatorial Mode of Interannual Variability

It is perhaps not surprising that the interannual variability of the Ridge configuration is dominated by an ENSO-like equatorial mode. Fig. 3 shows the empirical features of this dominant mode. In the first empirical orthogonal function (EOF) of monthly SST after removing the climatological seasonal cycle and long-term linear trend (Fig. 3a), the region with maximum variance is in the climatological cold tongue on the eastern side of the basin (cf. Fig. 2f in W21). In analogy to regions of Niño SST indices in the

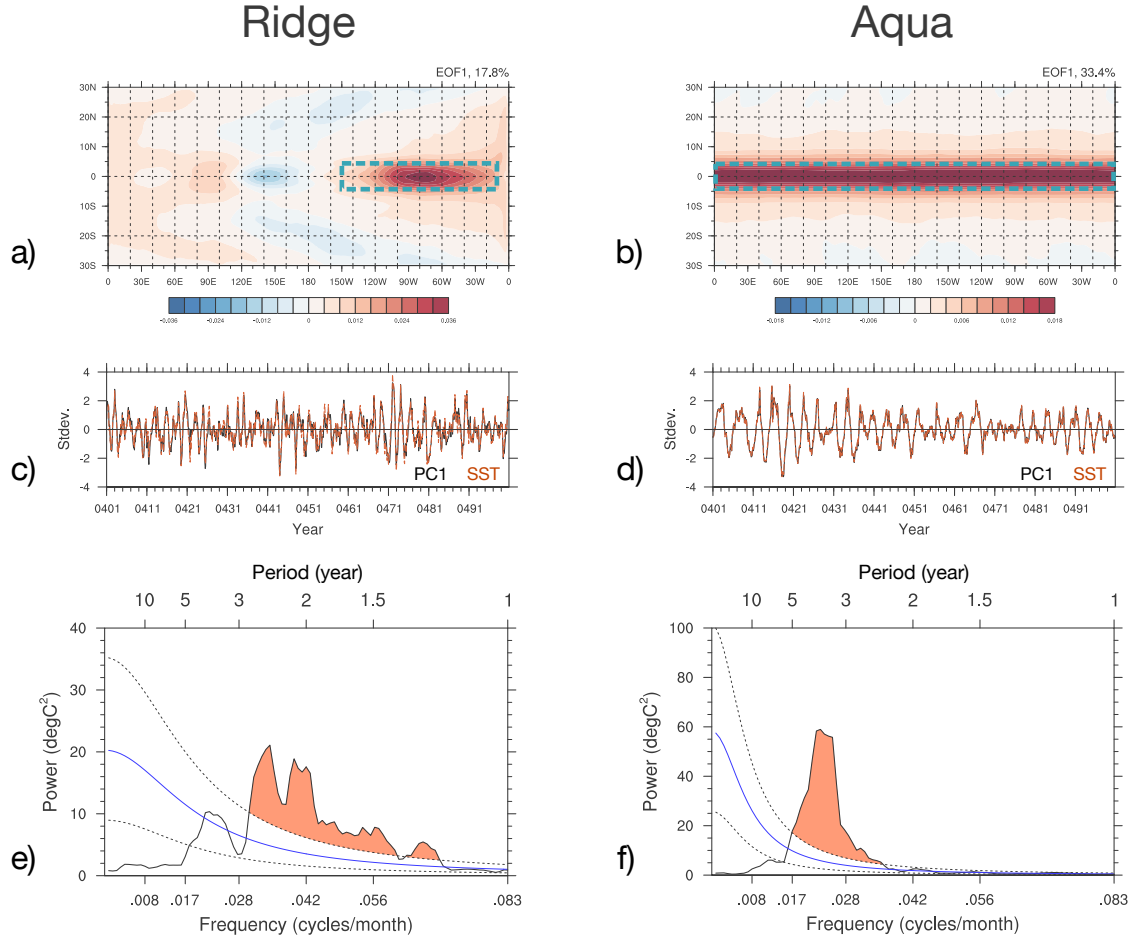


Figure 3. The leading mode of interannual variability in the equatorial region, using monthly averaged SST from Yr 401–500. The data is linearly detrended, and the climatological seasonal cycle is removed. (a–b) The first EOF, where the dashed blue box marks the equatorial region of dominating variability, 5°N–5°S, 150°W–10°W for Ridge (a) and 5°N–5°S for Aqua (b); (c–d) Standardized time series of the first PC (black) and SST (red) averaged over the boxed region in (a–b); (e–f) The power spectra of the SST time series. The orange shading indicates significant spectral peaks beyond 95% confidence level (i.e., $p < 0.05$).

Pacific, an indicative region is marked by the dashed blue box in Fig. 3a. The selection of this region is based on the pattern of SST varied, which also largely encompasses the climatological cold tongue with colder SST than the zonal average (cf. Fig. 2h in W21). As expected from the EOF methodology, the first principle component is closely associated with the average SST anomaly of this region (Fig. 3c). The periodicity of the monthly averaged SST anomaly is in the range of 1.5–3 years (Fig. 3e). The monthly averaged SST anomaly ranges between -2.50 – 2.96 °C, with standard deviation of 0.77 °C and skewness of 0.15 . The skewness towards warming qualitatively captures the observed feature of ENSO asymmetry (e.g., An & Jin, 2004). Notably, given the hemispheric symmetry of the model, the variance of monthly average SST anomaly in this indicative region peaks in both the boreal summer and winter seasons. The phase-locking to both seasons — instead of only boreal winter in the Pacific — likely contributes to the shorter period of this interannual mode, despite Ridge’s basin size being wider than the Pacific.

An exploration of these ENSO-like events in the Ridge configuration suggests processes comparable to the Pacific. Fig. 4 shows the ocean composite of warming years, and the strength of SST feedbacks as suggested by Planton et al. (2021). Using annually averaged ocean model output, the warming (cooling) years are defined as years where the annually averaged SST anomaly in the indicative region exceeds (drops below) one standard deviation. In the 100-year record, there are 17 warming years and 15 cooling years. The warming-year composite of sub-surface temperature anomaly 5°N – 5°S is shown in Fig. 4a. On the eastern side of the basin, the near-surface warming reaches down to ~ 100 m near the center of maximum warming around 90°W , and to ~ 300 m near the eastern boundary. On the western side of the basin, the sub-surface cooling along the climatological thermocline (cf. Fig. 2j in W21) suggests classical mechanisms for ENSO phase-switching (see e.g., review by C. Wang, 2018).

The strength of the feedback between SST and zonal wind stress — or the Bjerknes feedback — is shown in Fig. 4c. As in the Pacific, positive SST anomaly in the indicative region corresponds to relaxed easterly wind stress around the equator 180° – 90°W (cf. Fig. 2d in W21). The strength of the feedback between SST and surface heat flux is shown in Fig. 4e. East of 90°W , positive SST anomaly in the indicative regions corresponds to decreased surface heat flux into the ocean. On the other hand, the feedback is positive west of 90°W . This pattern largely comes from the combination of shortwave and latent heat anomalies (see Fig. S1 for components of surface heat flux). East of 100°W , where the wind stress anomaly is small (Fig. 4c), the positive SST anomaly enhances the latent heat flux into the atmosphere (Fig. S1e). Meanwhile, the relaxation of the easterlies west of 100°W likely contributes to the reduction of latent heat flux into the atmosphere, therefore warming the ocean. The opposing feedbacks in radiation, positive for shortwave and negative for longwave (Fig. S1a and c), suggest the role of clouds.

By design, the zonally symmetric Aqua configuration lacks the meridional boundary essential for aspects of ENSO dynamics related to oceanic wave reflection in the zonal direction. Somewhat surprisingly, its interannual variability is likewise dominated by an equatorial mode over the climatological cold belt of upwelling (Fig. 3b; cf. Fig. 2e in W21). Here the indicative region is extended accordingly (dashed blue box in Fig. 3b). The time series of SST anomaly varies at lower frequency than the Ridge configuration (Fig. 3d), with periodicity of 2–5 years (Fig. 3f). The average SST anomaly ranges between -2.68 – 2.55 $^{\circ}\text{C}$, with standard deviation of 0.81 $^{\circ}\text{C}$. Interestingly, with skewness of -0.12 , this equatorial mode of the Aqua configuration skews towards cooling. For the seasonal phase-locking, like the Ridge configuration, the variance of monthly average SST anomaly in the indicative region is bimodal in the annual cycle, peaking in both the summer and winter seasons.

As can be expected from the mean state (cf. Section 3.2 in W21), the ocean dynamics associated with this mode are substantially different from its ENSO-like counterpart in the Ridge configuration. Using the same definition for the annually averaged SST in the indicative region, there are 16 warming years and 16 cooling years in the 100-year record. To focus on the meridional structure, the warming-year composite of sub-surface temperature anomaly is zonally averaged (Fig. 4a). Very near to the equator in the latitude band 2°N – 2°S , the near-surface warming reaches beyond ~ 100 m. In the off-equatorial region 2° – 10°N/S , there is sub-surface cooling reaching beyond ~ 300 m. The persistence of these sub-surface cold anomalies through the annual cycle is likely essential for the phase-switching on the interannual time scale. As discussed in W21, since there is no geostrophically balanced meridional flow in the ocean interior for the Aqua configuration, meridional advection is attributed to parameterized eddy processes. The equatorward advection from $\sim 5^{\circ}$ – 10°N/S by meridional eddy velocity of $\sim O(1)$ cm s^{-1} yields a timescale of ~ 2 – 4 years, which likely contributes to the interannual phase-switching of this mode (cf. Fig. 8c in W21 for the residual overturning circulation).

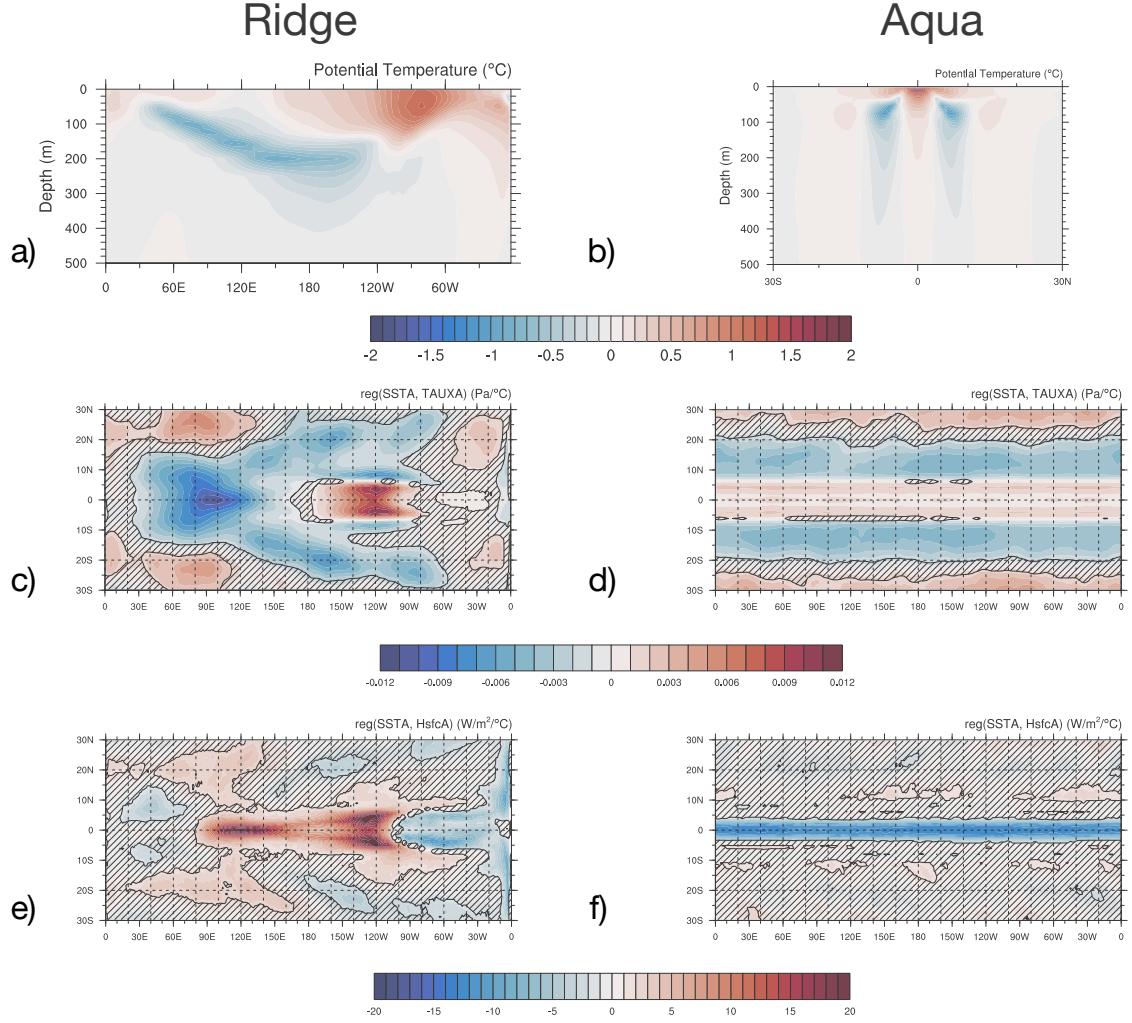


Figure 4. Composites of interannual warming events and SST feedbacks, using monthly averaged atmospheric data and annually averaged ocean potential temperature from Yr 401–500. The data is linearly detrended, and the climatological seasonal cycle is removed. (a–b) The composite of upper-ocean potential temperature anomaly of warming years (see text for definition), meridionally averaged 5°N – 5°S to show the zonal structure for Ridge (a), and zonally averaged to show the meridional structure between 30°N – 30°S for Aqua (b); (c–d) The strength of SST-zonal wind stress feedback, measured by the regression of SST anomaly on zonal wind stress anomaly; (e–f) The strength of SST-surface heat flux feedback, measured by the regression of SST anomaly on surface heat flux anomaly. The hatched areas in (c–f) mask out correlations below 95% confidence level (i.e., $p \geq 0.05$).

On the other hand, despite the contrast in the ocean interior, some aspects of the atmospheric component of Aqua’s interannual mode may be meaningfully compared to that of the Ridge configuration over the eastern side of the basin. Fig. 4d indicates the positive feedback between SST and zonal wind stress over the equatorial region 5°N–5°S. Although the regression here does not directly resolve the question of causality, the positive feedback can be reasonably expected. Warm SST anomalies in the cold belt, by reducing the meridional SST gradient, would lead to reduced off-equatorial easterly wind stress via geostrophic adjustment; meanwhile, reduced off-equatorial easterly wind stress is conducive to warmer equatorial SST via reduced upwelling. This positive feedback works to qualitatively similar effects as the canonical Bjerknes feedback, albeit impacting the meridional SST gradient instead of zonal. For the coupling between SST and surface heat flux anomalies (Fig. 4f), the negative feedback over the equatorial region is mostly through latent heat (Fig. S1f), where warmer equatorial SST enhances the latent heat flux into the atmosphere, and the relaxation of zonal wind by relatively small magnitude does not significantly counter this effect. In this aspect, Aqua’s equatorial cold belt may be regarded as behaving similarly to the eastern part of Ridge’s cold tongue east of 100°W (Fig. 4e). The opposing feedbacks in shortwave and longwave (Fig. S1b and d), making a relatively small contribution, take effect over the regions of climatological off-equatorial SST maxima (Fig. 4a in W21). These regions correspond to the ascending branch of the Hadley-like cells, conducive for clouds (Fig. 4d in W21).

In summary, the Ridge configuration is a reasonable model of the Pacific for both the mean state and its ENSO-like interannual variability, and similar variability exists in the Aqua model despite the lack of a meridional boundary. Contrary to Ridge’s zonal structure, Aqua’s essential ocean dynamics occur in the meridional direction, where off-equatorial subsurface temperature anomalies of opposite sign to the near-surface anomalies are likely important for the phase-switching. SST feedbacks over Ridge’s eastern cold tongue are partially maintained in Aqua’s equatorial cold belt, although with different mechanisms.

4 Discussion

Building on insights from previous works, fully coupled idealized models with resolution and physics similar to CMIP-class models are employed to investigate the dependence of MJO- and ENSO-like modes of variability on zonal asymmetry. We discuss the following aspects in the context of previous studies.

For the intraseasonal mode, when fully coupled ocean dynamics are included, the role of zonal asymmetry in enhancing more realistic MJO structures is mostly consistent with previous atmosphere-only idealized studies (Landu & Maloney, 2011; Maloney & Wolding, 2015; Das et al., 2019). However, somewhat contrary to the suggestion by Jiang, Maloney, and Su (2020), the propagation of the intraseasonal mode is not necessarily prohibited by the presence of double ITCZs in either the Ridge or Aqua configurations. Aside from model-dependent details in the atmospheric component, it remains to be seen if the interactive ocean coupling may have affected the propagation. On another note, the essential dynamics of MJO has been long debated in relation to moisture modes (e.g., Shi et al., 2018) or a dampened form of Kelvin waves (e.g., Kim & Zhang, 2021). Based on the contrast between the current Ridge and Aqua models, additional process-level diagnostics will likely provide more detailed perspectives on the distinction of this mode from Kelvin waves.

For the interannual mode, its existence in the equatorial cold belt on the coupled CESM Aqua planet prompts questions on model dependency, with relevance to realistic Earth configurations. Of the only other known documented example, the coupled Aqua model in Marshall et al. (2007) shows a leading mode of variability in the midlatitudes instead of the tropics. As discussed in W21, the differences in the model configuration

are abundant; here the resulting differences in variability again suggest the role of the mean state in constraining the variability. For the equatorial mode in CESM Aqua presently discussed, besides potential parallelisms to paleoclimate scenarios where the equatorial region had less land barriers (e.g., Li & Keller, 1999), relatable mechanisms involving the sub-surface anomalies in the meridional direction may be part of ENSO processes in the modern-day Pacific (e.g., “trade wind charging” in Chakravorty et al., 2020).

As concluding thoughts, we suggest a few future directions stemming from this exploratory work in the idealized, coupled modeling framework. For either mode of variability, detailed analysis of the energy budget of the atmospheric and/or oceanic components will shed light on the underlying processes in these two models. For the MJO-like intraseasonal mode, the role of the large-scale SST structure versus active coupling can be further isolated by prescribed-SST experiments. For the ENSO-like interannual mode, an extension of the current model hierarchy can help clarify the fundamental controls for the seasonal phase-locking by opening up the Drake Passage of Ridge and introducing interhemispheric asymmetry. For these suggested directions, the simplicity of idealized configurations can uniquely facilitate these types of experiments, and the interpretation of dynamical impacts. Furthermore, with increased model resolution, a wider range of scale interactions may be explored, including tropical cyclones.

Acknowledgments

We thank Antonietta Capotondi, Sarah Larson, Levi Silvers, Christine Shields, Bette Otto-Bliesner and many others for helpful discussions. The analysis of CCEWs benefited from diagnostic tools authored by Carl Schreck (<https://ncics.org/portfolio/monitor/mjo/>). Wu was supported by National Science Foundation (NSF) grant AGS1648629, the Advanced Study Program of NCAR, and the Junior Researcher Award of the Institute for Advanced Computational Science at Stony Brook University. Reed was supported by NSF grants AGS1648629 and AGS1830729. The National Center for Atmospheric Research (NCAR) is sponsored by the NSF under Cooperative Agreement 1852977. We acknowledge computing and data storage resources, including the Cheyenne supercomputer (doi:10.5065/D6RX99HX), provided by the Computational and Information Systems Laboratory (CISL) at NCAR.

The model case directories and the simulation outputs under analysis are available on CISL’s Globally Accessible Data Environment. The CESM source code is available at www.cesm.ucar.edu.

The first author dedicates this manuscript to the victims and responding officer fallen to the mass shooting at our neighborhood grocery store in Boulder, CO in March 2021.

References

- Ahn, M.-S., Kim, D., Kang, D., Lee, J., Sperber, K. R., Gleckler, P. J., . . . Kim, H. (2020). MJO propagation across the maritime continent: Are CMIP6 models better than CMIP5 models? *Geophysical Research Letters*, *47*(11), e2020GL087250.
- Ahn, M.-S., Kim, D., Sperber, K. R., Kang, I.-S., Maloney, E., Waliser, D., & Hendon, H. (2017). MJO simulation in CMIP5 climate models: MJO skill metrics and process-oriented diagnosis. *Climate Dynamics*, *49*(11), 4023–4045.
- An, S.-I., & Jin, F.-F. (2004). Nonlinearity and asymmetry of ENSO. *Journal of Climate*, *17*(12), 2399–2412.
- Battisti, D. S. (1988). Dynamics and thermodynamics of a warming event in a coupled tropical atmosphere–ocean model. *Journal of Atmospheric Sciences*, *45*(20), 2889–2919.
- Battisti, D. S., Vimont, D. J., & Kirtman, B. P. (2019). 100 years of progress in un-

- derstanding the dynamics of coupled atmosphere–ocean variability. *Meteorological Monographs*, 59, 8–1.
- Bayr, T., Wengel, C., Latif, M., Dommenges, D., Lübbecke, J., & Park, W. (2019). Error compensation of ENSO atmospheric feedbacks in climate models and its influence on simulated ENSO dynamics. *Climate dynamics*, 53(1), 155–172.
- Chakravorty, S., Perez, R. C., Anderson, B. T., Giese, B. S., Larson, S. M., & Pivotti, V. (2020). Testing the trade wind charging mechanism and its influence on ENSO variability. *Journal of Climate*, 33(17), 7391–7411.
- Chen, C., Cane, M. A., Wittenberg, A. T., & Chen, D. (2017). ENSO in the CMIP5 simulations: life cycles, diversity, and responses to climate change. *Journal of Climate*, 30(2), 775–801.
- Clement, A., DiNezio, P., & Deser, C. (2011). Rethinking the ocean’s role in the southern oscillation. *Journal of Climate*, 24(15), 4056–4072.
- Coppin, D., & Bony, S. (2017). Internal variability in a coupled general circulation model in radiative-convective equilibrium. *Geophysical Research Letters*, 44(10), 5142–5149.
- Danabasoglu, G., Lamarque, J.-F., Bacmeister, J., Bailey, D., DuVivier, A., Edwards, J., ... others (2020). The Community Earth System Model version 2 (CESM2). *Journal of Advances in Modeling Earth Systems*, 12(2), e2019MS001916.
- Das, S., Sengupta, D., & Chakraborty, A. (2019). The Madden-Julian Oscillation in an aquaplanet-like general circulation model with and without continents. *Journal of Advances in Modeling Earth Systems*, 11(5), 1459–1476.
- DeMott, C. A., Klingaman, N. P., & Woolnough, S. J. (2015). Atmosphere-ocean coupled processes in the Madden-Julian Oscillation. *Reviews of Geophysics*, 53(4), 1099–1154.
- Dias, J., & Kiladis, G. N. (2014). Influence of the basic state zonal flow on convectively coupled equatorial waves. *Geophysical Research Letters*, 41(19), 6904–6913.
- Dommenges, D., Haase, S., Bayr, T., & Frauen, C. (2014). Analysis of the slab ocean el nino atmospheric feedbacks in observed and simulated ENSO dynamics. *Climate dynamics*, 42(11), 3187–3205.
- Enderton, D., & Marshall, J. (2009). Explorations of atmosphere–ocean–ice climates on an aquaplanet and their meridional energy transports. *Journal of the Atmospheric Sciences*, 66(6), 1593–1611.
- Gill, A. E. (1982). *Atmosphere–ocean dynamics*. Elsevier.
- Grabowski, W. W. (2006). Impact of explicit atmosphere–ocean coupling on MJO-like coherent structures in idealized aquaplanet simulations. *Journal of the Atmospheric Sciences*, 63(9), 2289–2306.
- Hasselmann, K. (1976). Stochastic climate models part I. theory. *Tellus*, 28(6), 473–485.
- Hsu, P.-C., Li, T., & Murakami, H. (2014). Moisture asymmetry and MJO eastward propagation in an aquaplanet general circulation model. *Journal of Climate*, 27(23), 8747–8760.
- Hung, M.-P., Lin, J.-L., Wang, W., Kim, D., Shinoda, T., & Weaver, S. J. (2013). MJO and convectively coupled equatorial waves simulated by CMIP5 climate models. *Journal of Climate*, 26(17), 6185–6214.
- Hurrell, J. W., Holland, M. M., Gent, P. R., Ghan, S., Kay, J. E., Kushner, P. J., ... others (2013). The Community Earth System Model: A framework for collaborative research. *Bulletin of the American Meteorological Society*, 94(9), 1339–1360.
- Jiang, X., Adames, Á. F., Kim, D., Maloney, E. D., Lin, H., Kim, H., ... Klingaman, N. P. (2020). Fifty years of research on the Madden-Julian Oscillation: Recent progress, challenges, and perspectives. *Journal of Geophysical Research: Atmospheres*, 125(17), e2019JD030911.

- 449 Jiang, X., Maloney, E., & Su, H. (2020). Large-scale controls of propagation of the
450 Madden-Julian Oscillation. *npj Climate and Atmospheric Science*, 3(1), 1–8.
- 451 Kim, J.-E., & Zhang, C. (2021). Core dynamics of the MJO. *Journal of the Atmo-*
452 *spheric Sciences*, 78(1), 229–248.
- 453 Klingaman, N. P., & Demott, C. A. (2020). Mean state biases and interannual
454 variability affect perceived sensitivities of the Madden-Julian Oscillation to
455 air-sea coupling. *Journal of Advances in Modeling Earth Systems*, 12(2),
456 e2019MS001799.
- 457 Landu, K., & Maloney, E. D. (2011). Effect of SST distribution and radiative feed-
458 backs on the simulation of intraseasonal variability in an aquaplanet GCM.
459 *Journal of the Meteorological Society of Japan. Ser. II*, 89(3), 195–210.
- 460 Leroux, S., Bellon, G., Roehrig, R., Caian, M., Klingaman, N. P., Lafore, J.-P., ...
461 Tyteca, S. (2016). Inter-model comparison of subseasonal tropical variability
462 in aquaplanet experiments: Effect of a warm pool. *Journal of Advances in*
463 *Modeling Earth Systems*, 8(4), 1526–1551.
- 464 Li, L., & Keller, G. (1999). Variability in late cretaceous climate and deep waters:
465 evidence from stable isotopes. *Marine Geology*, 161(2-4), 171–190.
- 466 Maloney, E. D., & Sobel, A. H. (2007). Idealized hot spot experiments with a gen-
467 eral circulation model. *Journal of climate*, 20(5), 908–925.
- 468 Maloney, E. D., & Wolding, B. O. (2015). Initiation of an intraseasonal oscillation
469 in an aquaplanet general circulation model. *Journal of Advances in Modeling*
470 *Earth Systems*, 7(4), 1956–1976.
- 471 Marshall, J., Ferreira, D., Campin, J.-M., & Enderton, D. (2007). Mean climate and
472 variability of the atmosphere and ocean on an aquaplanet [Journal Article].
473 *Journal of the Atmospheric Sciences*, 64(12), 4270–4286.
- 474 Perez, C. L., Moore, A. M., Zavala-Garay, J., & Kleeman, R. (2005). A comparison
475 of the influence of additive and multiplicative stochastic forcing on a coupled
476 model of ENSO. *Journal of climate*, 18(23), 5066–5085.
- 477 Planton, Y. Y., Guilyardi, E., Wittenberg, A. T., Lee, J., Gleckler, P. J., Bayr, T.,
478 ... others (2021). Evaluating climate models with the CLIVAR 2020 ENSO
479 metrics package. *Bulletin of the American Meteorological Society*, 102(2),
480 E193–E217.
- 481 Schopf, P. S., & Suarez, M. J. (1988). Vacillations in a coupled ocean–atmosphere
482 model. *Journal of Atmospheric Sciences*, 45(3), 549–566.
- 483 Shi, X., Kim, D., Adames, Á. F., & Sukhatme, J. (2018). WISHE-moisture mode
484 in an aquaplanet simulation. *Journal of Advances in Modeling Earth Systems*,
485 10(10), 2393–2407.
- 486 Smith, R. S., Dubois, C., & Marotzke, J. (2006). Global climate and ocean circula-
487 tion on an aquaplanet ocean–atmosphere general circulation model. *Journal of*
488 *climate*, 19(18), 4719–4737.
- 489 Waliser, D., Sperber, K., Hendon, H., Kim, D., Maloney, E., Wheeler, M., ... others
490 (2009). MJO simulation diagnostics. *Journal of Climate*, 22(11), 3006–3030.
- 491 Wang, C. (2018). A review of ENSO theories. *National Science Review*, 5(6), 813–
492 825.
- 493 Wang, G., Dommengot, D., & Frauen, C. (2015). An evaluation of the CMIP3 and
494 CMIP5 simulations in their skill of simulating the spatial structure of SST
495 variability. *Climate Dynamics*, 44(1-2), 95–114.
- 496 Wheeler, M., & Kiladis, G. N. (1999). Convectively coupled equatorial waves: Anal-
497 ysis of clouds and temperature in the wavenumber–frequency domain. *Journal*
498 *of Atmospheric Sciences*, 56(3), 374–399.
- 499 Wu, X., Reed, K. A., Wolfe, C. L., Marques, G. M., Bachman, S. D., & Bryan, F. O.
500 (2021). Coupled Aqua and Ridge planets in the Community Earth System
501 Model. *Journal of Advances in Modeling Earth Systems*, e2020MS002418. doi:
502 10.1029/2020MS002418

503 Zebiak, S. E., & Cane, M. A. (1987). A model El Niño–Southern Oscillation.
504 *Monthly Weather Review*, 115(10), 2262–2278.